ELECTROCHEMISTRY

# On high-temperature evolution of passivation layer in Li–10 wt % Mg alloy via in situ SEM-EBSD

**Shirin Kaboli[1], Pierre Noel[1], Daniel Clément[1], Hendrix Demers[1], Andrea Paolella[1], Patrick Bouchard[2], Michel L. Trudeau[1]*, John B. Goodenough[3], Karim Zaghib[4]*†**



**Li–10 wt % Mg alloy (Li–10 Mg) is used as an anode material for a solid-state battery with excellent electrochemical performance and no evidence of dendrite formation during cycling. Thermal treatment of Li metal during manufacturing improves the interfacial contact between a Li metal electrode and solid electrolyte to achieve an all solid-state battery with increased performance. To understand the properties of the alloy passivation layer, this paper presents the first direct observation of its evolution at elevated temperatures (up to 325°C) by in situ scanning electron microscopy. We found that the morphology of the surface passivation layer was unchanged above the alloy melting point, while the bulk of the material below the surface was melted at the expected melting point, as confirmed by in situ electron backscatter diffraction. In situ heat treatment of Li-based materials could be a key method to improve battery performance.**

## INTRODUCTION

Li metal is one of the most attractive anode (negative electrode) materials for Li metal batteries owing to its ultrahigh theoretical specific capacity (3860 $mAhg^{-1}$) and lowest negative electrochemical potential (−3.040 V versus standard hydrogen electrode) (*1*). However, a number of challenges associated with Li-metal anodes have hindered commercial application, including Li-dendrite formation with potential safety hazards (*2*). Li dendrites may lead to internal short circuits in a battery and thus to a thermal runaway (*3*). Extensive studies have been carried out to develop alternative anode materials that overcome this problem for next-generation Li metal batteries. For example, Li alloy–based anode materials with increased structural and thermal stabilities are promising anode materials to replace pure Li metal anodes (*4*, *5*).

Among the numerous available Li alloy systems, the Li-Mg binary alloy has been considered a superior candidate (*6*, *7*), owing to several properties, including a phase stability over a broad composition range (*6*, *7*) [α body-centered cubic (BCC) phase up to 30 atomic % Li, based on the Li-Mg phase diagram (*8*, *9*)], higher melting point for improved battery safety (*8*, *9*), and improved wettability of the electrolyte (*10*, *11*). The Li-Mg alloy offers a better stripping-plating of Li ions and dense interphase layer and a higher current density compared to the pure Li anode (*7*). Furthermore, the Li-rich Li-Mg formulation provides increased surface stability owing to a robust passivation layer protecting the anode from excessive side reactions with the electrolyte (*7*). In addition, heat treatment of the Li metal during manufacturing improves the physical contact between the anode and solid electrolyte, which yields a higher battery performance (*12*–*14*). Thus, characterization of the passivation layer at high temperatures is imperative to improve the cycle life of an all-solid-state battery (*15*), which is critically dependent on the solid-electrolyte interface layer.

However, our literature survey shows a lack of detailed information on the physical metallurgy of Li alloys, including the grain morphology, crystal orientation distribution, and surface chemistry at high temperatures. This is not unexpected as the operations with Li metal, and its alloys at high temperatures are challenging owing to their extreme reactivities in environments containing $O_2$, $N_2$, $CO_2$, water, and air, even in trace amounts (*16*, *17*). It is impossible to have a fresh Li surface as a surface passivation layer forms immediately after the fabrication processes (extrusion and lamination in the case of Li sheets), unless working under noble gases such as Ar. In addition, the sample preparation and handling are tedious as various Li oxide compounds ($Li_2O$, $Li_2O_2$, $Li_2CO_3$, and LiOH) spontaneously form on the surface (*16*). Thus, Li-based materials are considered one of the most challenging systems for in situ scanning electron microscopy (SEM) studies at high temperatures.

In situ electron microscopy at high temperatures has enabled real-time studies of dynamic processes in materials in various physics and chemistry research fields (*18*) and is an invaluable characterization method for in situ imaging and analysis of dynamic changes at material surfaces during heating/cooling over a wide field of view at a nanometer spatial resolution (*19*, *20*). Our group has used in situ SEM as a suitable technique to study all-solid battery materials, specifically Li metal anodes, in the battery operation temperature range of 60° to 100°C (*21*–*24*) for decades. Here, we present the first in situ observations of the morphology and chemical changes of the passivation layer of a Li-rich Li-Mg alloy above the alloy melting point. This study advances our understanding of the metallurgy of Li at high temperatures (above the melting point) and the development of advanced battery materials to avoid local fusion of Li anodes (*25*) and thermal runaway during short circuits (*26*).

## RESULTS AND DISCUSSION

We cycled two all-solid batteries, with a Li–10 weight % (wt %) Mg anode (see table S1 for the alloy composition) and a pure Li anode. Both batteries had a $LiFePO_4$ (LFP) cathode and solid polymer electrolyte (SPE) with the same cell design. We cycled both batteries at 80°C, an

[1]Hydro-Québec's Center of Excellence in Transportation Electrification and Energy Storage, Varennes, QC J3X 1S1, Canada. [2]Hydro-Québec's Center of Excellence in Transportation Electrification and Energy Storage, Shawinigan, QC G9N 7N5, Canada. [3]Texas Materials Institute and Materials Science and Engineering Program, University of Texas at Austin, Austin, TX 78712, USA. [4]Department of Materials Engineering, McGill University, Montreal, QC H3A 0C5, Canada.
*Present address: Department of Materials Engineering McGill University, Montreal, QC, Canada.
†Corresponding author. Email: karim.zaghib@mcgill.ca

operating voltage of 2.0 to 3.65 V under a constant current at two C rates (nC rate: cycling in 1/n h): C/24 and C/3. The cell composition is found in the Supplementary Materials. Figure S1 shows the schematic of the cell design. Figure 1 shows the cycling curves providing cell capacity and efficiency during cycling. On the basis of these results, in comparison to the cell with the pure Li anode, the cell with the Li-Mg anode had an excellent electrochemical performance with capacity of 156 mAh/g and a high coulombic efficiency of 99.2%. We performed postmortem analysis on the cycled Li-Mg/SPE/LFP battery in cross section. The results of postmortem energy-dispersive spectroscopy (EDS) analysis are shown in Fig. 1 (E to M). The secondary-electron (SE) image in (Fig. 1E) shows a smooth interface between the Li-Mg anode and the SPE. We carefully surveyed the entire length of the cell and found no evidence of dendrite formation during cycling.

We thus carried out a series of in situ heating tests on the Li-Mg alloy inside an SEM. The surface of the as-received Li-Mg sheets is generally covered with a very thin protective coating in addition to the original passivation layer (*27*). As surface layers might affect the heating of the material (*28*), we imaged a freshly cut microtomed surface in a cross-section view. Figure S2 shows an SE image of the sample surface and corresponding EDS at room temperature (RT)

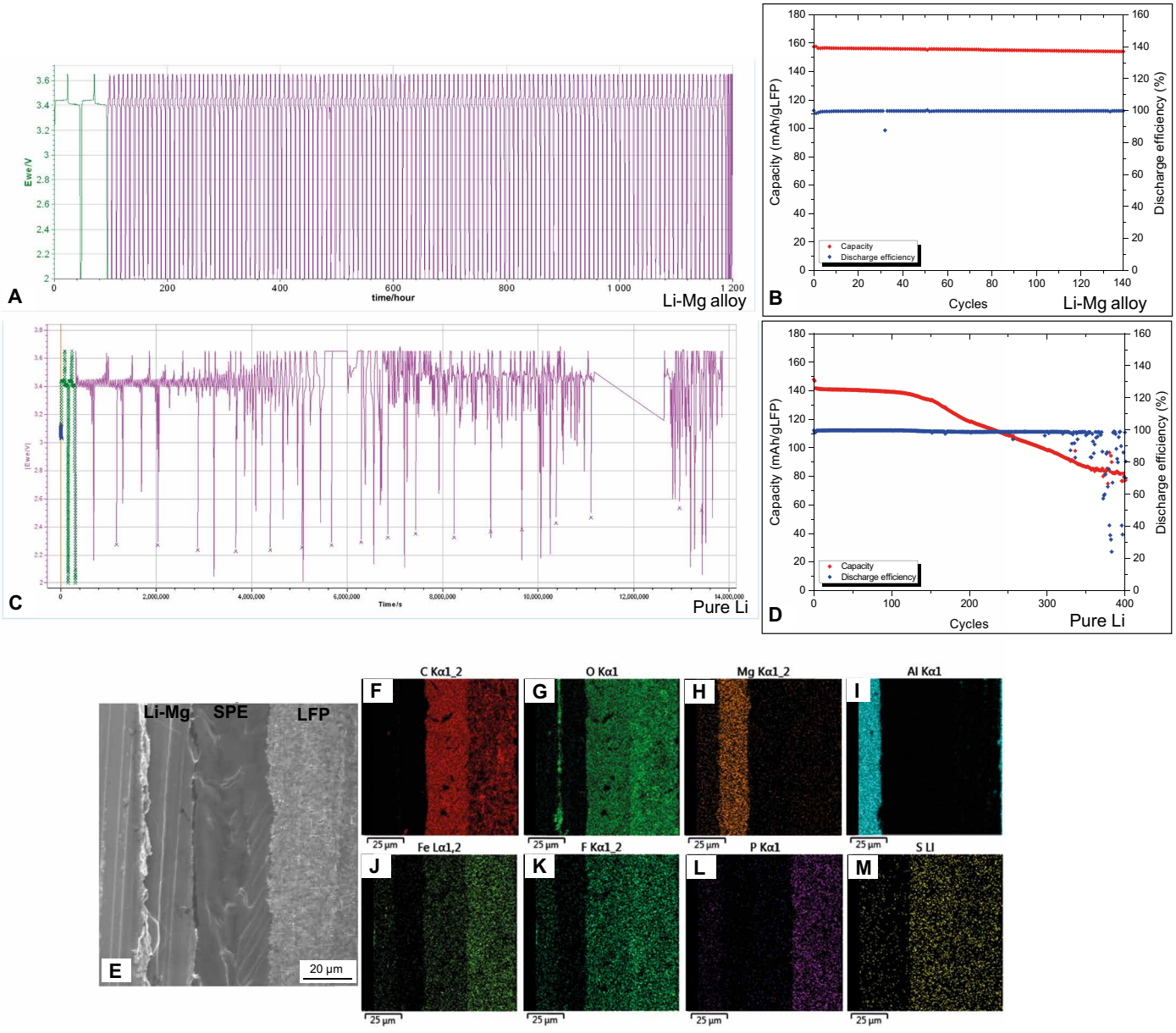


**Fig. 1. Cycling results for two all-solid cells with a Li-Mg anode and pure Li anode at 80°C.** (**A** and **C**) Plot of Ewe (V) as a function of cycling time (hours) for two C rates (C/24 in green and C/3 in purple). (**B** and **D**) Cell capacity and discharge efficiency as a function of number of cycles. In comparison to the pure Li cell, the Li-Mg cell provides an excellent electrochemical performance with capacity of ~156 mAh/g and a very high coulombic efficiency of 99.2%. (**E** to **M**) Postmortem EDS analysis on the cross section of the cycled Li-Mg cell. We observed a smooth interface between the Li-Mg anode and the SPE. We did not detect dendrites across the entire length of the cell.

immediately after the cryomicrotomy. The grain boundaries were not visible in the cross section after the cryomicrotomy. The EDS results showing high amounts of O and C and a small amount of Li confirm that the passivation layer formed immediately after the cryomicrotomy. The formation of a surface passivation layer is attributed to the formation of ice on the surface under cryogenic conditions. The microtomed surface at RT was inevitably contaminated by $H_2O$ and $CO_2$ even under continuous Ar flushing in a dry room.

We performed two heating experiments on the same sample. Figure S3 shows the sample and stage temperature profiles during the experiments. The temperature was increased to ~325°C in the first run. After cooling, we increased the temperature to ~325°C in the second run, followed by cooling to RT. We did not control the cooling rate as the sample was cooled inside the SEM under vacuum. Movie S1 shows the primary stage of heating, which ended with a sudden cracking of the surface layer at ~275°C and loss of the area of interest. The cracking occurred irregularly across the entire surface. The surface cracking could be attributed to the pressure increase from the melt underneath the solid surface after the alloy melting point. We selected a second stable area of interest with a few surface cracks from the previous step for imaging. Movie S2 shows the microstructure evolution during the first heating test. The temperature range where the movie was acquired is indicated on the temperature profile in fig. S3. Movie S2 shows a continuous expansion of the sample during heating to the maximum temperature (fig. S4). The surface remained solid during heating as the surface passivation layer contained Li oxide ($Li_2O$; melting point: 1432°C), Li hydroxide (LiOH; melting point: 462°C), and $Li_2CO_3$ (melting point: 723°C), compounds with higher melting points than that of the Li–10 wt % Mg alloy [~185°C; (*8*, *9*)]. During cooling, we observed a sudden formation of surface topography at ~180°C followed by a rapid cracking of the surface at ~170°C and the appearance of a dark phase on the surface. Figure 2 (A to C) shows the surface microstructure and corresponding EDS results after the first heating test. Figure 2B shows a higher-magnification view of the dark phase indicated by the red square in Fig. 2A. According to the EDS results, a high amount of O existed on the surface (bright areas) with low levels of Li and Mg, while a considerably lower level of O and high levels of Li and Mg existed in the dark regions. Therefore, the dark phase was a solidified Li-Mg melt originating from underneath the surface, as indicated in

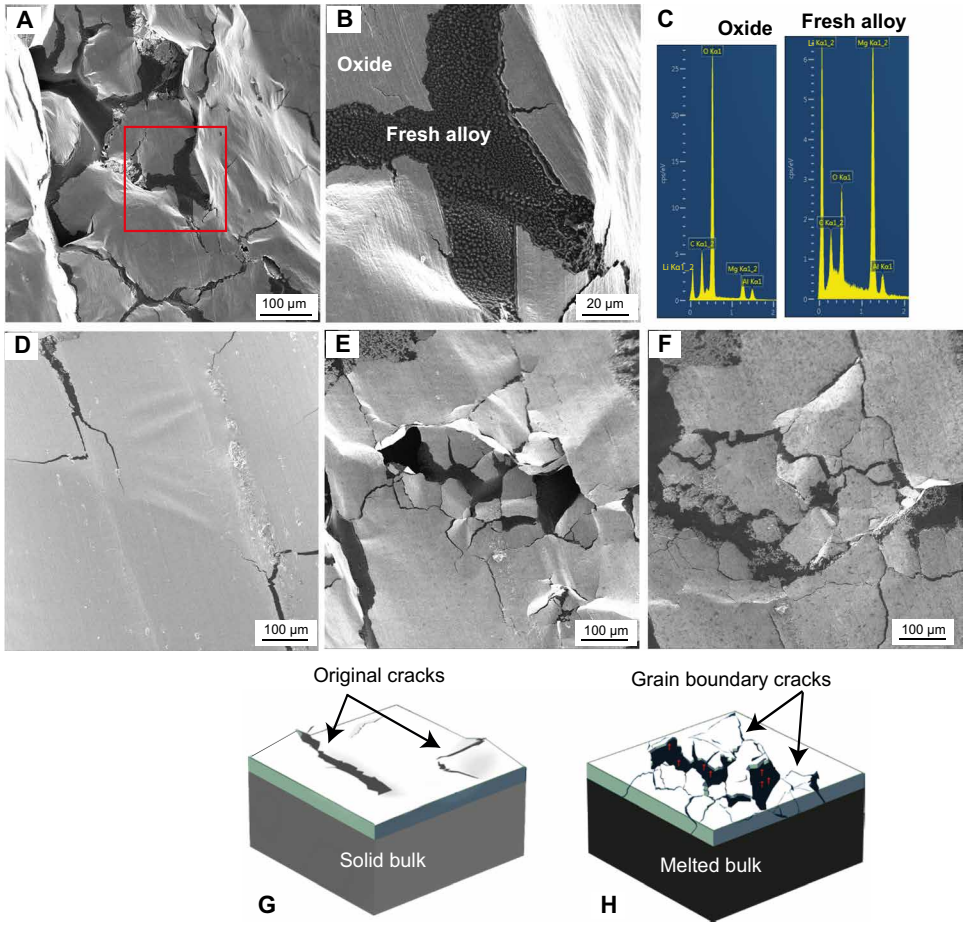


**Fig. 2. The results of microstructure studies after in situ heating tests.** (**A** and **B**) The secondary electron images and (**C**) corresponding energy-dispersive spectra from the Li–10 wt % Mg surface after the first heating experiment. The bright regions contain the surface passivation layer, while the dark regions contain the fresh Li–10 wt % Mg alloy after melting and solidification. (**D** to **F**) The secondary electron images of the same area at the beginning of heating (D) after first cool down (E) and after second cool down (F). Comparing (E) and (F) shows that the size and organization of the grains and the distribution of the grain boundaries were completely changed in the second heating experiment. Surface topography also decreased after the second heating test. (**G** and **H**) The three-dimensional schematic representation of the sample at the beginning of heating (G) and formation of localized melt at the grain boundaries (H). The surface morphology mimics the results shown in (D) and (E), respectively.

Fig. 2B. In addition, we observed similar levels of C and a small amount of Al in both areas (Fig. 2C). The cracking of the surface at the grain boundary regions is the result of the liquid to solid phase transformation below the surface passivation layer. If the heat treatment temperature is lower than the melting point of Li-Mg alloy, the cracks do not form during cooling.

Movie S3 shows the microstructure evolution of the same area shown in movie S1 during the second heating test. We indicate the temperature range where the movie was acquired on the temperature profile in fig. S3. Movie S3 shows that the fresh Li-Mg alloy at the original grain boundaries was partially melted during heating followed by a continuous movement of the melted boundaries on the surface. We observed severe surface topography and expansion of the dark phase at the grain boundaries, which occurred at ~170°C.

These heating tests reveal that the surface cracks associated with the formation of fresh Li-Mg alloy had a grain boundary morphology different from that of the original large-scale cracks on the surface at the beginning of the test. Figure 2 (D to F) shows the same area after the first and second heating tests to compare the microstructures. The surface at the beginning of test with original surface cracks is shown in (Fig. 2D). The surface morphology after the second cooling (Fig. 2F), including the distribution of grains and positions of grain boundaries, was different from that after the first cooling (Fig. 2E).

To investigate the origin of the newly formed cracks, we repeated the heating experiment in a plane view to monitor the evolution of the original grain boundaries on the surface. Figure 3 (A and B) shows the grain morphologies at 300°C and after cooling to RT. We observed the dark phase containing the fresh Li-Mg alloy at the grain boundaries, as indicated by the red arrows in (B). Therefore, these cracks occurred at the original grain boundaries in the passivation layer. The underlying melt spread across these boundaries during the solidification. Figure 3 (C to I) shows the results of EDS mapping in a grain containing both the passivation layer and fresh Li-Mg at the grain

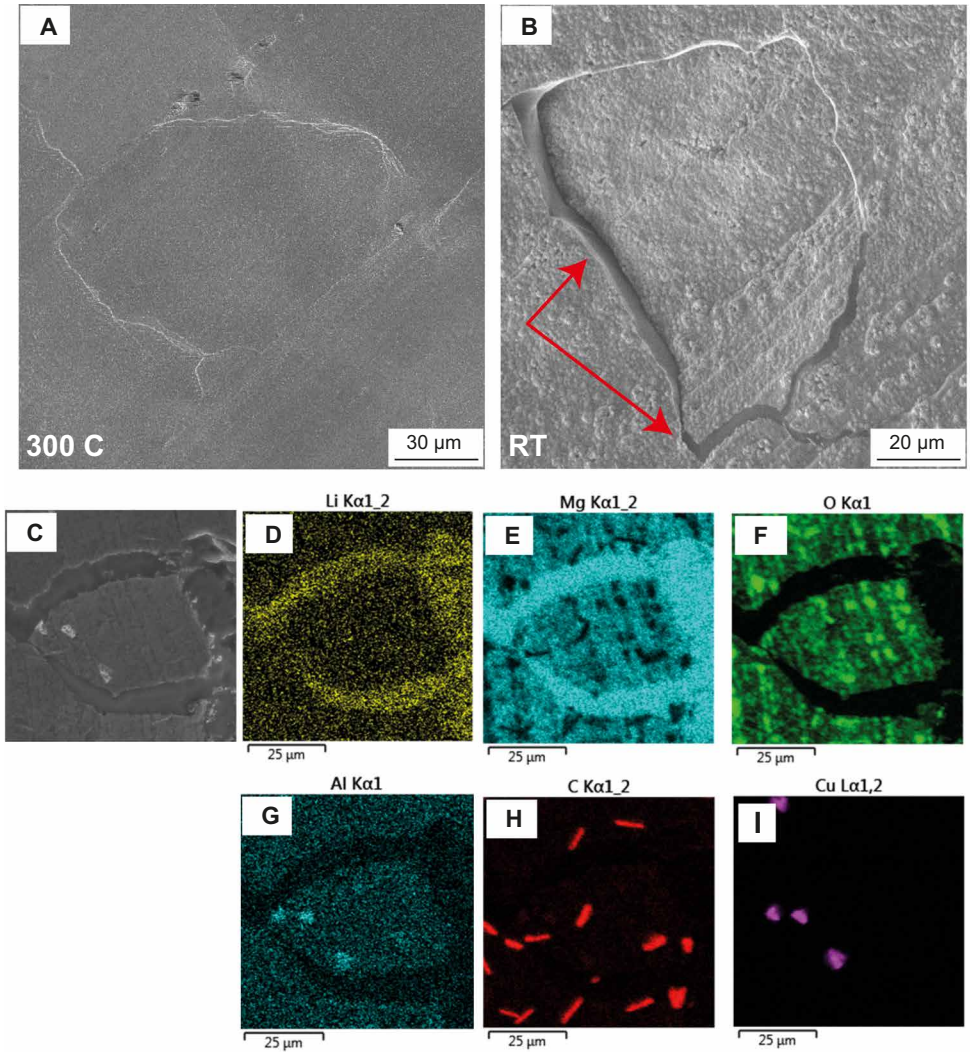


**Fig. 3. The results of plane-view heating experiment on Li–10 wt % Mg alloy.** (**A** and **B**) The secondary electron images of the same grain at 300°C (A) and RT (B). The dark phase containing fresh Li–10 Mg phase appeared at the original grain boundaries indicated by red arrows in (B). (**C** to **I**) The results of postmortem EDS mapping on the Li–10 wt % Mg sample after two heating tests. The grain boundaries showed fresh Li–10 wt % Mg alloy and depleted of O, while the passivation layer showed a homogeneous distribution of Al. We also observed contamination by C and Cu impurities. The passivation layer in (D) does not show obvious distribution of Li since the concentration of Li is higher in the solidified phase at the grain boundaries after melting and solidification.

boundaries. The maps show that the grain-boundary phase was O-depleted and contained Li and Mg, consistent with the results in Fig. 2C. We also observed C and Cu contaminations in the passivation layer. We observed a homogeneous distribution of Al in the passivation layer, but not in the grain boundaries. The particles in Fig. 3C exhibited Al and Cu contaminations. The sample was contaminated by the formation of impurities at high temperatures owing to the high reactivity of Li near its melting point (*29*). Possible sources of contamination could be the holder or contaminants already present in the microscope chamber.

For a better understanding of the evolution of a passivation layer during cooling, the cracking of the grain boundaries in movie S2 is illustrated in Fig. 2 (G and H). This cracking is known as liquation cracking, which can occur in the partially melted zone during the solidification of the liquid material (*30*, *31*). Grain boundaries are mechanically weak regions owing to the segregation of impurities and alloying elements and thus exhibit a higher cracking risk under mechanical stress. After cracking, the melted material underneath the surface filled the open space in the grain boundaries and subsequently solidified during cooling (Fig. 2H).

For a better understanding of the dynamical change of the relation between the surface and bulk of the material, we performed in situ electron backscatter diffraction (EBSD) mapping. Figure 4 (A to D) shows band contrast maps and inverse pole figure (IPF-Z) coloring maps obtained from the same region at RT, 50° and 150°C, and RT after cooling. The color scheme represents the crystal orientation distribution of Li grains in the sample. The higher-temperature maps (50° and 150°C) have a lower resolution than that of the original RT map because of the need to use a larger step size (27 μm) for mapping at high temperatures with a smaller mapping time. In addition, more zero solutions (black regions) existed in the 50° and 150°C maps owing to the lower qualities (low signal-to-noise ratio) of the EBSD patterns acquired at high temperatures. Zero solutions refer to the EBSD patterns that did not index to any known solutions available in the EBSD Aztec software database for crystal orientation determination. The lower-pattern quality at the higher temperature may be attributed to a higher background signal as the EBSD detector is sensitive to the infrared light emitted from the hot sample. The zero solution regions in the RT map after cooling were attributed to the absence of EBSD patterns owing to a severe surface topography of the solidified surface.

We observed similar morphologies of the Li grains (size, shape, and crystal orientation distribution) at RT, 50° and 150°C. It is not possible to calculate the misorientation angles (residual stress zones) in the grains (represented by gradual changes in color) with certainty owing to the low resolution of the high-temperature maps (Fig. 4, B and C) compared to that of the RT map (Fig. 4A). However, we observed Li grains with a completely new morphology from the RT map after cooling. Figure 4D shows two Li grains with new crystal orientations presented in green and yellow (see the color scheme), which confirms that we melted the material below the passivation layer on the surface and formed new grains after the solidification.

The maximum information depth of backscattered electrons in a pure Li metal sample at 30 keV is ~350 nm (*32*), estimated by Monte Carlo (MC) simulations with MC x-ray software (*33*). According to Bessette *et al.* (*17*), the thickness of the passivation layer on an extruded Li-Mg alloy is ~250 nm. Therefore, although the surface passivation layer was solid near the Li melting point, the EBSD signal originated from the material below the surface, which was melted. Thus, we were not able to obtain any EBSD patterns at temperatures near the Li melting point (~185°C) (*34*, *35*).

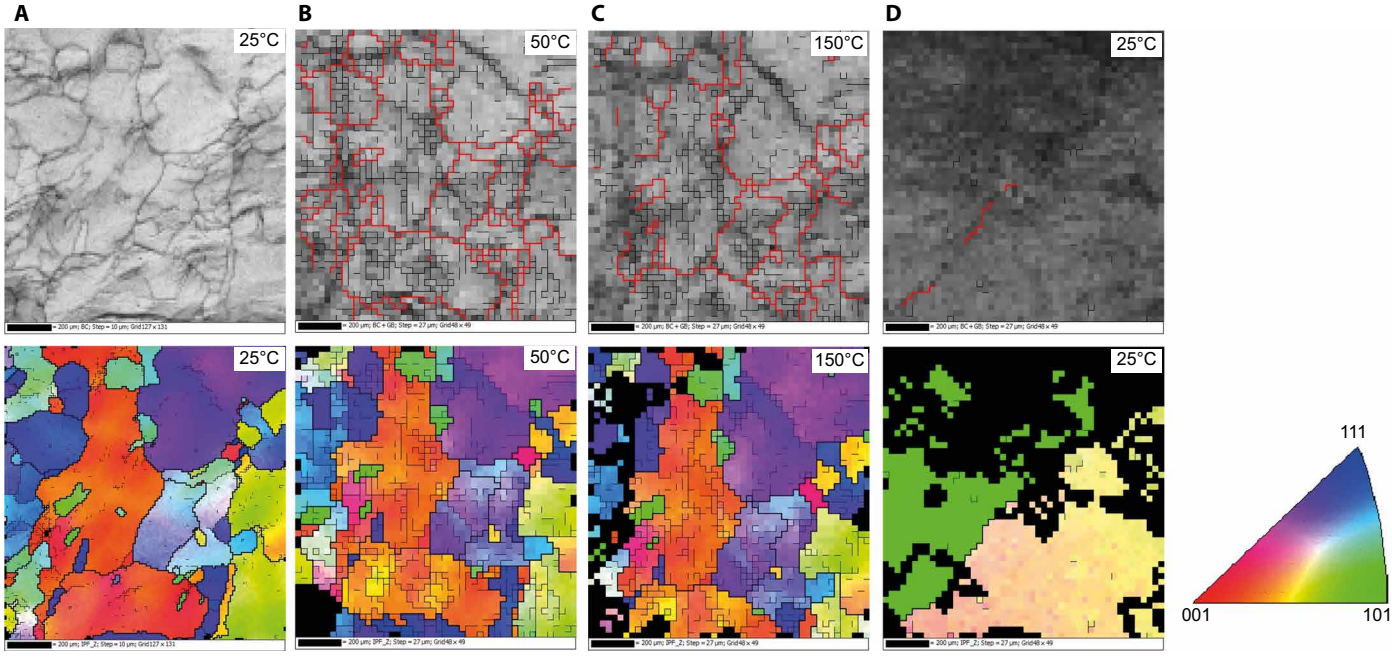


**Fig. 4. The results of in situ EBSD mapping on the Li–10 Mg sample.** (**A** to **D**) The band contrast maps and inverse pole figure (IPF-Z) coloring maps at RT (A), 50°C (B), 150°C (C), and RT after cool down (D). The surface morphology (size, shape, and distribution of grains) remained almost unchanged up to the alloy melting point. However, after melting and solidification, new grain morphology with new crystal orientations indicated by new color key formed on the surface. The new Li grains were formed when the melted alloy solidified at the theoretical melting point temperature of the alloy (~185°C).

In summary, we used the Li–10 wt % Mg alloy as the anode material for an all-solid battery with excellent electrochemical performance. To study the possible changes in the passivation layer on this alloy with temperature, we performed heat treatment tests on a Li–10 wt % Mg alloy sample up to 325°C with in situ SEM. The results of the imaging show that the surface passivation layer remained solid throughout the test, while the material underneath the surface was melted and solidified at the surface grain boundaries. The EDS results show that the solidified alloy was fresh and depleted of O-, C-, and other-contaminants, while the rest of the passivation layer contained impurities. The EBSD crystal orientation mapping shows the formation of new grains on the surface after melting that had new crystal orientations. On the basis of the above observations, the residual passivation layer on the Li-Mg alloy surface after a heat treatment above the alloy melting point was composed of the original passivation later, in addition to the solidified pure Li-Mg material at the grain boundary regions. The advantages of a solid passivation layer of this alloy on the electrochemical performance of all-solid battery with a Li-Mg anode include the elimination of dendrite formation, a lower risk of local fusion of Li at the electrolyte/anode interface, and therefore a safer battery operation. Thus, in situ heat treatment and observation in a SEM could be a useful technique to understand the structure and properties of the passivation layer and its relation to the metallurgy of new Li alloys with preferred crystal orientations. For future work, we will investigate the structural stability and chemical concentration of different alloying elements at the anode/SPE interface during cycling.

## MATERIALS AND METHODS

We cycled all-solid battery with Li–10 wt % Mg alloy as the anode material. The cathode material is a LFP with active material (5.053 mg/cm$^2$), 58.22% of LFP, 10.2% black acetylene, 3.1% VGCF, 3.5% LiFSI, and 24.5% polyether. The electrolyte is a polyether-based polymer with LiFSI as salt. The cell design is schematically shown in fig. S1.

We carried out in situ heating tests on a Li-rich Li-Mg alloy sample in a high-vacuum Schottky electron microscopy (chamber pressure ~ 10 to 5 Pa at RT). We monitored various dynamic phenomena including the morphology of Li grains by continuous SE imaging. We performed in situ EBSD to map the crystal orientation distributions during the heating and cooling. We also present the changes in surface chemistry using postmortem EDS on the samples at RT.

We used an extruded Li–10 wt % Mg alloy (nominal composition) sheet (thickness: 263 μm; LTE-Hydro-Québec, Shawinigan, QC). The melting point of this alloy is higher (~185°C) than a pure Li metal (~180.5°C) (*8*) (see Supplementary Materials for specifications of additives and impurities in this material in table S1). The Li sheets had a very thin (nanometer) organic residual coating on the top surface formed in the fabrication process. The sample handling and surface preparation were performed in a dry room with a dew point of ~−53°C to minimize the contamination of the sample with moisture and subsequent formation of LiOH and $Li_2CO_3$. The SEM observation was also performed inside a dry room. We performed experiments in cross-section and plane views for imaging and only plane view for EBSD. We used cryomicrotomy with liquid Ar (Leica Biosystems RM2265) to prepare the cross-section sample for observation inside the SEM. We stacked five 1-cm by 1-cm square sheets together in the form of a sandwich sample, which was enclosed between two clean Ni foils in the preparation for the cryomicrotomy. The microtomed sample was then placed vertically in the cross-section holder with the microtomed surface facing the electron beam. The exposed Li surface was continuously flushed by Ar gas during the sample handling and transfer from the microtome to the SEM to minimize the sample contamination. For the plane-view imaging, we did not perform surface preparation on the sample. For the EBSD, we performed ion beam milling on a 1-cm by 1-cm square sample. We used a flat ion milling system with an IM-4000 Plus Hitachi High Technologies to obtain a flat surface suitable for EBSD. We carried out ion beam milling in two steps, each for 10 min at a beam energy of 4 keV, rotation of 360°, and sample tilt of 85° with a break of 30 min between the steps to avoid temperature increase in the sample. Immediately after the milling, the sample was transferred onto the 70°-pretilted EBSD holder with a carbon tape as a support and placed into the SEM.

We also performed the same heat treatment on a pure Li metal sample. The preparation and experimental procedure is similar to above (see results in fig. S5).

### In situ heating setup

The in situ heating setup with cross-section and EBSD sample holders was designed and manufactured in-house (Hydro-Québec). We performed annealing using a resistance furnace mounted on the SEM stage. The sample holders for cross-section imaging and EBSD mapping were attached to the furnace. We used Ni foils to protect the parts of the cross-section holder (Al-based) in contact with the Li melt to avoid possible damage or contamination of the holder. We used a chiller and liquid nitrogen cold trap to reduce the sample contamination and cool the stage during the heating tests. We stopped the heat treatment at 325°C to prevent any possible damage to the SEM stage components. For temperature measurements, we used two thermocouples to continuously monitor the sample and stage temperatures. The estimated error in the sample temperature reading was ~±5°C. We placed a heat shield on top of the sample holder with a small opening to enable the detection of the secondary electrons. The temperature was increased stepwise to ensure temperature uniformity in the sample and sufficient time for sample drift corrections. For heating, we used a Eurotherm EPC3008 controller and iTools software (version 9.79). This software is equipped with an OPC scope acquisition module, which enabled the control of the temperature through the controller.

### In situ imaging

We used a MIRA3 TESCAN SEM equipped with a standard EDS detector (Oxford Instruments) and a windowless extreme EDS detector (Oxford Instruments), which can detect Li, and a NordlysNano EBSD system. The large chamber of this microscope provides an ideal platform for the installation of the heating module for in situ heating experiments. The vacuum pressure inside the SEM chamber was ~$10^{-5}$ Pa at RT and was increased up to ~$8 \times 10^{-3}$ Pa owing to the outgassing of the sample, furnace, and stage at high temperatures close to the melting point. We performed in-beam SE imaging at low magnification, beam energy of 4 keV, and operation distance of ~14 to 15 mm. We performed imaging at the center of the sample where the temperature was considered homogeneous. The time step between images was typically 2 to 30 s, depending on the kinetics of the changes in surface morphology as a function of the temperature. The electron beam scanning time for each image was 2 s. We did not detect any motion or drift of the solid/liquid interface

over the scanning. The brightness, contrast, and stigmatism were continuously adjusted during the imaging. We also adjusted the stage position to correct for any sample drift due to expansion or shrinkage of the material. After the tests, the images were used to construct videos to observe the various dynamic phenomena in the sample.

We used MATLAB computer programming to construct videos from the images. The temperature (°C) of the sample is indicated in red in the upper-left corners in the videos. The temporary horizontal lines in the videos during the primary stages of heating are undesired noise from the power supply interfering with the beam scanning the surface. We also experienced radiation from the melted regions, which temporarily blocked the SE detector and EBSD camera.

### In situ SEM-EBSD mapping

We used a NordlysNano EBSD system with the Aztec acquisition software (Oxford Instruments) to perform EBSD mapping on the sample. To protect the EBSD detector from thermal and gas emissions, we placed a third thermocouple near the EBSD camera to monitor the temperature and carry out necessary adjustments to prevent damage to the camera. We mapped the area of interest at RT. The sample was then heated to the target temperature (50°, 150°, and 200°C). For the 200°C test, we did not have any problems with the melt flow from the sample tilted at 70°. Before the EBSD acquisition, we waited approximately 30 min to ensure temperature uniformity in the sample. We performed the EBSD mapping at 30 keV in the high-beam current mode with step sizes of 10 μm for the maps acquired at RT and 25 μm for the maps acquired at high temperatures. For the EBSD pattern acquisition, we used 4 × 4 binning and high-camera gain. We applied dynamic background subtraction to the EBSD patterns. We performed noise reduction on raw maps to decrease the number of black pixels (zero solutions). For indexation of the EBSD patterns, we used the data for the pure Li crystal with a BCC lattice structure. We list the challenges to perform high-temperature SEM-EBSD experiments below (*20*).

1) Hardware: The SEM stage has temperature sensitive components (plastic or polymer-based materials) that can be damaged at high temperature. Therefore, it is necessary to implement a cooling system in the SEM to keep the temperature of the stage in the safe range (typically below 60°C).

2) Hardware: The EBSD phosphorous screen needs to be protected at high temperature to prevent any possible damage. We monitored the temperature near the phosphorous screen with an additional thermocouple to ensure the temperature stays in the safe range.

3) Software: Preparation of a flat sample is essential to perform EBSD mapping because EBSD pattern acquisition is very sensitive to the surface topography. During heating, the sample develops surface topography as temperature increases. During the cool down, the cracking of the grain boundaries and solidification of the melt at these regions result in a severe surface topography (Fig. 2A). Surface topography gives low quality for the EBSD patterns that leads to zero solutions for the pattern indexation and high mean angular deviation (MAD) values for the solutions.

4) Software: The high-temperature EBSD patterns have lower quality (lower signal-to-noise ratio) that may be attributed to a higher background signal as the EBSD detector is sensitive to the infrared light emitted from the hot sample. Low-quality maps give low indexation rate for the EBSD patterns (more zero solutions) and also higher MAD values for the solutions. Low indexation rate and high MAD values increase uncertainty in orientation determination.

5) Working conditions: Even with the presence of a cooling system, it is not advisable to perform high-temperature EBSD mapping over an extended period of time (for example, overnight mapping) without supervision. As a result, we had to use a larger step size for mapping at high temperature to perform mapping during a reasonable working time with supervision. Larger step size results in drawbacks including lower spatial resolution map and loss of details (Fig. 4, B to D).

## SUPPLEMENTARY MATERIALS

Supplementary material for this article is available at http://advances.sciencemag.org/cgi/content/full/6/50/eabd5708/DC1

## REFERENCES AND NOTES


1. W. Xu, J. Wang, F. Ding, X. Chen, E. Nasybulin, Y. Zhang, J.-G. Zhang, Lithium metal anodes for rechargeable batteries. *Energ. Environ. Sci.* **7**, 513–537 (2014).
2. C. Fang, X. Wang, Y. Meng, Key issues hindering a practical lithium-metal anode. *Trends Chem.* **1**, 152–158 (2019).
3. Y. Takeda, O. Yamamoto, N. Imanishi, Lithium dendrite formation on a lithium metal anode from liquid, polymer and solid electrolytes. *Electrochemistry* **84**, 210–218 (2016).
4. M. N. Obrovac, V. L. Chevrier, Alloy negative electrodes for Li-ion batteries. *Chem. Rev.* **114**, 11444–11502 (2014).
5. C.-M. Park, J.-H. Kim, H. Kim, H.-J. Sohn, Li-alloy based anode materials for Li secondary batteries. *Chem. Soc. Rev.* **39**, 3115–3141 (2010).
6. Z. Shi, M. Liu, D. Naik, J. L. Gole, Electrochemical properties of Li–Mg alloy electrodes for lithium batteries. *J. Power Sources* **92**, 70–80 (2001).
7. L.-L. Kong, L. Wang, Z.-C. Ni, S. Liu, G.-R. Li, X.-P. Gao, Lithium–Magnesium alloy as a stable anode for Lithium–Sulfur battery. *Adv. Funct. Mater.* **29**, 1808756 (2019).
8. W. Gasior, Z. Moser, W. Zakulski, G. Schwitzgebel, Thermodynamic studies and the phase diagram of the Li-Mg system. *Metallurg. Mater. Trans. A* **27**, 2419–2428 (1996).
9. A. A. Nayeb-Hashemi, J. B. Clark, A. D. Pelton, The Li-Mg (Lithium-Magnesium) system. *Bullet. Alloy Phase Diag.* **5**, 365–374 (1984).
10. J. Wang, H. Wang, J. Xie, A. Yang, A. Pei, C.-L. Wu, F. Shi, Y. Liu, D. Lin, Y. Gong, Y. Cui, Fundamental study on the wetting property of liquid lithium. *Energy Storage Mater.* **14**, 345–350 (2018).
11. S.-H. Wang, J. Yue, W. Dong, T.-T. Zuo, J.-Y. Li, X. Liu, X.-D. Zhang, L. Liu, J.-L. Shi, Y.-X. Yin, Y.-G. Guo, Tuning wettability of molten lithium via a chemical strategy for lithium metal anodes. *Nat. Commun.* **10**, 4930 (2019).
12. S. Li, H. Wang, W. Wu, F. Lorandi, J. F. Whitacre, K. Matyjaszewski, Solvent-processed metallic Lithium microparticles for Lithium metal batteries. *ACS Appl. Energy Mater.* **2**, 1623–1628 (2019).
13. Z. Liang, D. Lin, J. Zhao, Z. Lu, Y. Liu, C. Liu, Y. Lu, H. Wang, K. Yan, X. Tao, Y. Cui, Composite lithium metal anode by melt infusion of lithium into a 3D conducting scaffold with lithiophilic coating. *Proc. Natl. Acad. Sci.* **113**, 2862–2867 (2016).
14. Y. Shen, Y. Zhang, S. Han, J. Wang, Z. Peng, L. Chen, Unlocking the Energy capabilities of lithium metal electrode with solid-state electrolytes. *Joule* **2**, 1674–1689 (2018).
15. E. Peled, S. Menkin, Review—SEI: Past, present and future. *J. Electrochem. Soc.* **164**, A1703–A1719 (2017).
16. M. M. Markowitz, D. A. Boryta, Lithium metal-gas reactions. *J. Chem. Eng. Data* **7**, 586–591 (1962).
17. S. Bessette, P. Hovington, H. Demers, M. Golozar, P. Bouchard, R. Gauvin, K. Zaghib, In-situ characterization of lithium native passivation layer in a high vacuum scanning electron microscope. *Microsc. Microanal.* **25**, 866–873 (2019).
18. F. Banhart, *In-Situ Electron Microscopy at High Resolution* (World Scientific, 2008), pp. 318.
19. E. A. Torres, A. J. Ramírez, *Science and Technology of Welding and Joining* (Taylor & Francis, 2011), vol. 16, pp. 68–78.
20. R. Podor, G. I. N. Bouala, J. Ravaux, J. Lautru, N. Clavier, Working with the ESEM at high temperature. *Mater Charact* **151**, 15–26 (2019).
21. M. Golozar, P. Hovington, A. Paolella, S. Bessette, M. Lagacé, P. Bouchard, H. Demers, R. Gauvin, K. Zaghib, In situ scanning electron microscopy detection of carbide nature of dendrites in Li–Polymer batteries. *Nano Lett.* **18**, 7583–7589 (2018).
22. M. Golozar, A. Paolella, H. Demers, S. Bessette, M. Lagacé, P. Bouchard, A. Guerfi, R. Gauvin, K. Zaghib, In situ observation of solid electrolyte interphase evolution in a lithium metal battery. *Commun. Chem.* **2**, 131 (2019).
23. P. Hovington, M. Lagacé, A. Guerfi, P. Bouchard, A. Mauger, C. M. Julien, M. Armand, K. Zaghib, New lithium metal polymer solid state battery for an ultrahigh energy: Nano C-LiFePO$_4$ versus Nano Li$_{1.2}$V$_3$O$_8$. *Nano Lett.* **15**, 2671–2678 (2015).
24. S. Kaboli, H. Demers, A. Paolella, A. Darwiche, M. Dontigny, D. Clément, A. Guerfi, M. L. Trudeau, J. B. Goodenough, K. Zaghib, Behavior of solid electrolyte in Li-Polymer

battery with NMC cathode via in-situ scanning electron microscopy. *Nano Lett.* **20**, 1607–1613 (2020).
25. M. Zhang, L. Liu, A. Stefanopoulou, J. Siegel, L. Lu, X. He, M. Ouyang, Fusing phenomenon of Lithium-ion battery internal short circuit. *J. Electrochem. Soc.* **164**, A2738–A2745 (2017).
26. D. P. Finegan, E. Darcy, M. Keyser, B. Tjaden, T. M. M. Heenan, R. Jervis, J. J. Bailey, R. Malik, N. T. Vo, O. V. Magdysyuk, R. Atwood, M. Drakopoulos, M. DiMichiel, A. Rack, G. Hinds, D. J. L. Brett, P. R. Shearing, Characterising thermal runaway within lithium-ion cells by inducing and monitoring internal short circuits. *Energ. Environ. Sci.* **10**, 1377–1388 (2017).
27. N. Delaporte, Y. Wang, K. Zaghib, Pre-treatments of Lithium foil surface for improving the cycling life of Li metal batteries. *Front. Mater.* **6**, 267 (2019).
28. W. J. Kroll, Melting and evaporating metals in a vacuum. *Trans. Electrochem. Soc.* **87**, 571 (1945).
29. W.-J. Zhang, A review of the electrochemical performance of alloy anodes for lithium-ion batteries. *J. Power Sources* **196**, 13–24 (2011).
30. S. Kou, Solidification and liquation cracking issues in welding. *JOM* **55**, 37–42 (2003).
31. A. R. VieiraNunes, A. Zeemann, L. H. deAlmeida, The contribution of impurities to unexpected cold cracks in a thick C-Mn steel plate. *J. Mater. Res. Technol.* **8**, 4364–4373 (2019).
32. N. Brodusch, K. Zaghib, R. Gauvin, Electron backscatter diffraction applied to lithium sheets prepared by broad ion beam milling. *Microsc. Res. Tech.* **78**, 30–39 (2015).
33. R. Gauvin, P. Michaud, MC X-Ray, a new Monte Carlo programfor quantitative X-ray microanalysis of real materials. *Microsc. Microanal.* **15**, 488–489 (2009).
34. W. Wisniewski, C. Rüssel, An experimental viewpoint on the information depth of EBSD. *Scanning* **38**, 164–171 (2016).
35. W. Wisniewski, S. Saager, A. Böbenroth, C. Rüssel, Experimental evidence concerning the significant information depth of electron backscatter diffraction (EBSD). *Ultramicroscopy* **173**, 1–9 (2017).

**Acknowledgments:** We thank J.B.G. for editing our publication. We thank É. Leroux for her assistance with the schematic figures in the manuscript. We also thank F. Gendron, K. Amouzegar, and J. Pronovost for their help in cycling the all-solid batteries. **Funding:** This research was funded by Hydro-Québec's Center of Excellence in Transportation Electrification and Energy Storage, Varennes, Québec. **Author contributions:** S.K. and M.L.T. designed the plot for the heating experiments. S.K. and P.N. designed the set up and conducted the heating experiments and characterization work. P.B. performed the cycling tests. D.C. helped with cryomicrotomy sample preparation. H.D., A.P., M.L.T., J.B.G., and K.Z. helped with the interpretation of the results. S.K. wrote the manuscript. All authors discussed the results and commented on the manuscript. **Competing interests:** The authors declare that they have no competing interests. **Data and materials availability:** All data is available in the main text or the Supplementary Materials except for the raw EBSD data that is a property of Hydro-Québec. Additional data related to this paper may be requested from the authors.

Submitted 29 June 2020
Accepted 22 October 2020
Published 9 December 2020
10.1126/sciadv.abd5708

**Citation:** S. Kaboli, P. Noel, D. Clément, H. Demers, A. Paolella, P. Bouchard, M. L. Trudeau, J. B. Goodenough, K. Zaghib, On high-temperature evolution of passivation layer in Li–10 wt % Mg alloy via in situ SEM-EBSD. *Sci. Adv.* **6**, eabd5708 (2020).

ScienceAdvances

# On high-temperature evolution of passivation layer in Li–10 wt % Mg alloy via in situ SEM-EBSD

Shirin Kaboli, Pierre Noel, Daniel Clément, Hendrix Demers, Andrea Paolella, Patrick Bouchard, Michel L. Trudeau, John B. Goodenough, and Karim Zaghib

*Sci. Adv.* **6** (50), eabd5708. DOI: 10.1126/sciadv.abd5708







*Science Advances* (ISSN 2375-2548) is published by the American Association for the Advancement of Science. 1200 New York Avenue NW, Washington, DC 20005. The title *Science Advances* is a registered trademark of AAAS.